Energy & Environmental Science

Accepted Manuscript

This article can be cited before page numbers have been issued, to do this please use: K. Cheng, S. Tu, B. Zhang, W. Wang, X. Wang, Y. Tan, X. Chen, C. Li, C. Li, L. Wang and Y. Sun, *Energy Environ. Sci.*, 2024, DOI: 10.1039/D4EE00407H.

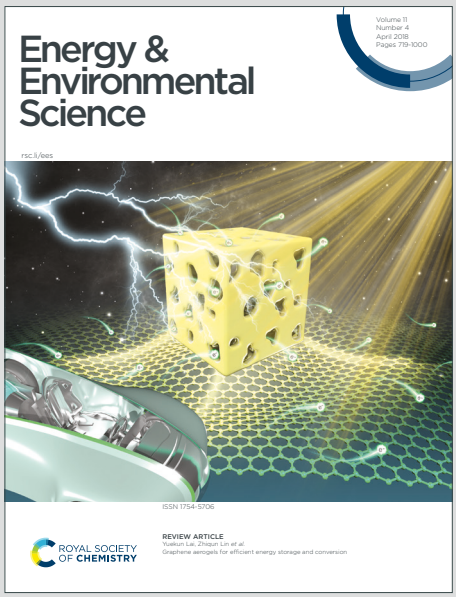

ROYAL SOCIETY OF CHEMISTRY

rsc.li/ees

View Article Online
DOI: 10.1039/D4EE00407H

Broader context

SEI is formed through the decomposition of the electrolyte components adsorbed on the inner Helmholtz plane (IHP) of the anode surface. Scientifically, the constitution and spatial configuration of specific adsorption behavior, which is significantly affected by the composition and properties of electrolyte components and substrate, plays a significant role in SEI formation. Despite considerable progress in electrolyte engineering, the mechanism of how the substrate interacts with the electrolyte and its effect on SEI remains unexplored. In this work, we revealed the vital role of active material interphase engineering in SEI design by regulating the preferable adsorption and reduction of electrolyte components for high-performance Si-based anodes in lithium-ion batteries (LIBs). With an ultrathin P interphase layer, FEC was preferentially adsorbed and decomposed on the SiO_x surface, which enabled the formation of dense Li_3P/LiF dual-layer SEI featuring high Li^+ conductivity but high stability and prolonged the cycling and rate capability of LIBs. This work has shed light on utilizing material-electrolyte interfacial interaction regulation to tailor the composition and mechanical properties of SEI. It may boost advanced SEI design for high-energy density LIBs with fast charging capability.

Material-electrolyte interfacial interaction enabling formation of inorganic-rich solid electrolyte interphase for fast-charging Si-based lithium-ion batteries

Received 00th January 20xx,
Accepted 00th January 20xx

DOI: 10.1039/x0xx00000x

Kai Cheng[†,a,b]; Shuibin Tu[†,a]; Bao Zhang[a]; Wenyu Wang[a]; Xiaohong Wang[a]; Yucheng Tan[a]; Xiaoxue Chen[a]; Chunhao Li[a]; Chenhui Li[b]; Li Wang[c]; and Yongming Sun[*,a]

Abstract: Solid-electrolyte interphase (SEI) with high stability and high Li^+ conductivity is highly desirable for Si-based lithium-ion batteries with high energy density and superior fast charging capability. Here, we proposed constructing a superior SEI by regulating the interaction between electrolyte components and anode surfaces to achieve the above goal. With combined experimental and theoretical studies, we demonstrated that the P-based layer could selectively adsorb fluoroethylene carbonate (FEC, a common electrolyte solvent) to form a robust, thin, and dense Li_3P/LiF-dominated SEI with high ionic conductivity on SiO_x particles. The SiO_x with a uniform 6 nm-thick P layer (SiO_x@P) delivered excellent electrochemical cycling stability (1050 mAh g^{-1}, 83.3% capacity retention for 1000 cycles at 1.0 *C*). Our Ah-level $LiNi_{0.6}Co_{0.2}Mn_{0.2}O_2$||$SiO_x$@P pouch cell demonstrated stable cycling with a high energy density (410 Wh kg^{-1} and 780 Wh L^{-1} at 0.2 *C*), along with an exceptional fast charging capability. It exhibited the capability to charge up to 86.5 % of its capacity within 15 minutes and demonstrated 83.8% capacity retention after 250 cycles at a 4 *C* charging rate. This achievement offers a unique insight into SEI formation, providing new opportunities to construct advanced SEI for Si-based anodes toward high energy density fast charging LIBs.

1. Introduction

Silicon suboxides (SiO_x, $0 < x < 2$) were regarded as promising anode materials for the realization of high-energy-density LIBs due to their high theoretical capacity (1695–4200 mAh g^{-1}), low equilibrium potential (0.2–0.4 V *vs.* Li/Li^+, all potentials are referred to the Li/Li^+ redox couple) and abundant resources.[1-4] However, the practical application of SiO_x anodes was limited by their inferior electrochemical performance, including poor cycling stability and unsatisfied rate capability. The significant volume change (118–300%) during the lithiation/delithiation processes of SiO_x and the brittle mechanical property of solid electrolyte interphase (SEI) cause the continuous SEI cracking/repairing and consumption of electrolytes, which becomes one of the dominating reasons for inferior cycling stability, low Coulombic efficiency (CE) and poor rate capability of SiO_x anodes.[5, 6] Construction of a mechanically robust and chemically /electrochemically stable SEI with high ion conductivity can suppress the adverse effects caused by volume changes, thereby improving the electrochemical performance of the SiO_x anode.[7-9] Specifically, a SEI with high ion conductivity is instrumental in achieving the superior fast-charging capability of LIBs with high energy density.

SEI on SiO_x surfaces formed via the reduction of regular carbonate electrolytes often possesses a solvent-swelling loose structure, which is responsible for its fragile property and electrochemical/chemical instability.[10] An ideal SEI for high-volume-expansion SiO_x anodes should possess robust mechanical stability, good electronic insulation, and compact structure,[11] which hinder the repeated fracture of SEI and the continuous parasitic reactions between active material and electrolyte during cycling. In the past years, inorganic species (e.g., LiF, Li_2CO_3, and Li_2O) have been long confirmed as practical SEI components that can enhance the SEI stability due to their high mechanical strength (e.g., shear modules of 55.1 GPa for LiF) and low solubility in comparison to organic SEI species.[12, 13] Till now, numerous studies have been devoted to constructing inorganic-rich SEI through engineering electrolyte components and Li^+ solvation structures, such as the use of highly fluorinated electrolyte additives (e.g., fluoroethylene carbonate, FEC) and design of high salt concentration electrolytes.[14-17] In addition to the electrolyte properties, the electrode surface accessible to the electrolyte also has a crucial role in facilitating the formation of advanced SEI. Species in the electrolyte, including anions (such as NO_3^-) and polar molecules (such as FEC), can be specifically absorbed in the inner Helmholtz plane (IHP) of the electrode/electrolyte interface and be preferentially decomposed to produce inorganic species during SEI formation.[18-20] The inorganics often dominate the SEI properties, including ionic conductivities, mechanical strength, and chemical/electrochemical stability. Current electrolyte designs heavily look at the portion of inorganic in SEI, while not always working well. In comparison to the content, the distribution of the inorganic species in SEI may be more critical for the electrochemical performance of the anode. The uneven distribution of large inorganic domains often makes inferior properties of the SEI.[13, 21] Therefore, it is urgent to develop new mechanisms /approaches for designing uniform, dense, and stable inorganic-rich SEI structures with high ion conductivity.

In this work, we investigated the adsorption behavior of FEC in IHP on different material surfaces (including Si, SiO, and red-P) through molecular dynamics (MD) simulations and density functional theory

[a.] *Wuhan National Laboratory for Optoelectronics, Huazhong University of Science and Technology, Wuhan 430074, China*
[b.] *State Key Laboratory of Material Processing and Die & Mould Technology, School of Materials Science and Engineering Huazhong University of Science and Technology, Wuhan 430074, Hubei, China*
[c.] *Institute of Nuclear & New Energy Technology, Tsinghua University, Beijing 100084, China.*
† These authors contributed equally to this work.
Electronic Supplementary Information (ESI) available: [details of any supplementary information available should be included here. See DOI: 10.1039/x0xx00000x
Corresponding author: yongmingsun@hust.edu.cn

(DFT) calculation. It was revealed that FEC could be characteristically adsorbed in the IHP of red-P compared to Si or SiO_x. We experimentally fabricated SiO_x@P composites featuring a red-P nanolayer (~ 6 nm) firmly bonded on the SiO_x surface by a simple chemical balling approach. Red-P nanolayer accelerated the FEC reduction at ~ 1.25 V and *in-situ* converted to Li_3P at ~ 0.7 V,[22-25] producing symbiotic Li_3P/LiF-rich SEI with enhanced mechanical durability, high electrochemical stability, and ionic conductivity on SiO_x anode. As a result, the SiO_x@P anode delivered a high average cyclic Coulombic efficiency of 99.9%, good cycling stability with a high reversible capacity (1050 mAh g^{-1}), 83.3% capacity retention after 1000 cycles at 1.0 *C*, and excellent rate capability. Paired with a high-loading $LiNi_{0.6}Co_{0.2}Mn_{0.2}O_2$ (NCM622) cathode, an Ah-level pouch cell showed stable cycling with a high energy density (410 Wh kg^{-1} and 780 Wh L^{-1} at 0.2 *C*), superior fast charging capability (4 *C* charge to 86.5 % of its capacity at 0.2 *C*, 83.8% capacity retention for 250 cycles at 4 *C*). We highlight the importance of characteristic adsorption and interaction between the active material interface and electrolyte component in SEI component and structure regulation for high-performance Si-based anodes, which provide new avenues of material interface engineering for advanced high-energy density LIBs with fast charging capability.

2 Results and Discussion

2.1 Surface-Engineering Manipulated Active Molecule Adsorption

The molecules/ions from the electrolyte within IHP adjacent to the anode surface are reduced, and the corresponding products participate in SEI formation.[26] Scientifically, this process relies on the properties and composition of the electrolyte components and substrate, which together determine the component and spatial configuration of specific adsorption behavior.[27-29] Despite significant progress in electrolyte engineering, the mechanism of how the substrate interacts with the electrolyte and its effect on SEI remains unexplored. Here, we investigated the impact of different substrates on the structure and properties of SEI in carbonate electrolytes containing FEC additives, which was widely regarded as an active

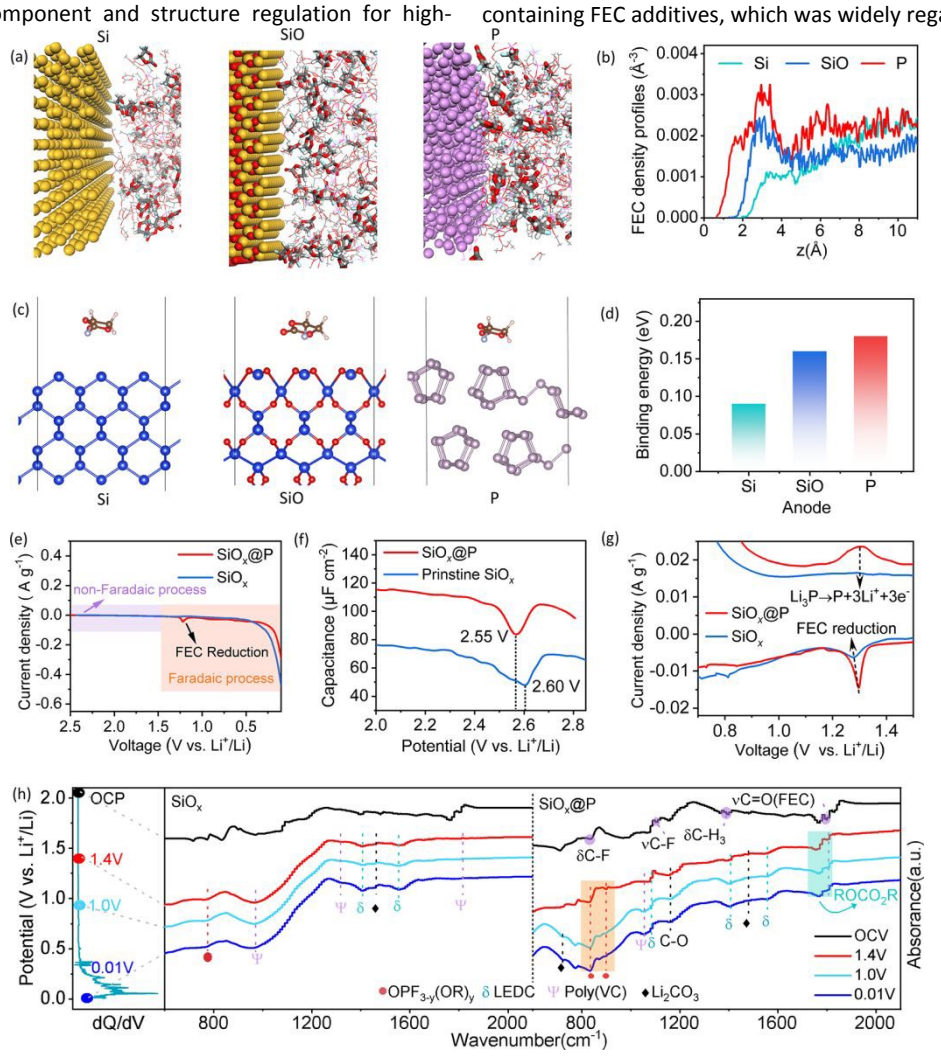

Fig.1 (a) MD simulations and (b) FEC adsorption density profiles on the Si and P surfaces. (c) DFT calculations and (d) binding energy of FEC molecules adsorption on different material surfaces. (e) The LSV curves of the SiO_x@P and bare SiO_x anodes. (f) The non-Faradaic capacitance-potential curves for the SiO_x@P and bare SiO_x electrodes at 2.0 – 3.0 V. (g) Initial CV curves of the SiO_x@P and bare SiO_x electrodes at a scanning rate of 0.01 mV s^{-1} between 0.7–1.5 V. (h) dQ/dV plot of the SiO_x@P electrode and *ex*-situ FTIR spectra of the SiO_x@P and bare SiO_x electrodes at different potential during the first discharge process.

film-forming species and could be reduced to inert polyvinylidene carbonate (poly-VC) and high modulus LiF to enhance SEI stability.[30] Increasing the chance of FEC molecules being absorbed into IHP is expected to improve the utilization rate of FEC, thereby assisting in

forming a robust SEI on the alloy-type anode. In this study, the adsorption behavior of FEC molecules on different surfaces of alloy-type materials (including Si, SiO, and red-P) was investigated using MD simulations and DFT calculation. The adsorption density profile of FEC molecules in the parallel orientation on the slabs of Si, SiO, and P surfaces (Fig. 1a, b) and the binding energy on those surfaces toward FEC (Fig. 1c, d) were considered. The results showed that the FEC adsorption density on the red-P surface was higher than that on the other Si surface components (Fig. 1b), and the binding energy between the red-P and FEC (0.18 eV) was higher than those between Si (0.09 eV) and SiO (0.17 eV) surfaces (Fig. 1d). To reveal the adsorption behavior mechanism of FEC in IHP and its impact on SEI formation, experimentally, we investigated the electrochemical behavior of the SiO_x@P (see details of the fabrication in the supporting information, Figs. S1 and S2, and Note S1) and bare SiO_x anodes in FEC-containing electrolyte. The electrolyte consisting of 1.3 M $LiPF_6$ in ethylene carbonate (EC) / ethyl methyl carbonate (EMC) (EC / EMC = 3 / 7 by volume fraction) with 20 wt.% FEC, and 1 wt.% VC additives (LP20, Table S1, Supporting Information) were used for each test, otherwise stated. The linear sweep voltammetry (LSV) curve demonstrated that both the non-Faradaic double layer capacitance adsorption process and Faradaic decomposition process in the IHP took place in the range of 1.4–2.5 V and 0–1.4 V, respectively (Fig. 1e). Alternating current (AC) voltammetry was utilized to observe the adsorption behavior, and the non-Faradaic capacitance-potential curves were calculated based on the data collected (Fig.1f). It showed that both the potential and capacitance of the SiO_x@P at the potential of zero charge (PZC) changed compared to the bare SiO_x (2.55 *vs*. 2.60 V for PZC), revealing their difference of FEC adsorption features in the IHP.[31, 32]

The Fourier transform infrared spectroscopy (FTIR) spectrum of the SiO_x@P electrode at OCV demonstrated four new peaks discerned corresponding to the deformation of the C-F bond (v C-F, at ~ 1100 cm^{-1}), the stretching vibration of the C-F bond (δ C-F, at ~ 1160 cm^{-1}), the skeletal breathing of the C-H bond (δ C-H, at ~ 1360 cm^{-1}) and the symmetrical stretching of the C-O bond (v C-O, at ~1840 cm^{-1}) of the FEC molecule. This observation underscores the enhanced FEC adsorption compared to the bare SiO_x electrode (Fig. S3a).[33-35]. The corresponding FTIR signal of the SiO_x@P electrode consistently exceeded that of the bare SiO_x electrode with the potential decrease from OCV to 1.4V (Fig. S3b). When referring to the Faradaic decomposition process, in the initial lithiation process of the SiO_x@P anode, the FEC molecule displayed a more noticeable reduction peak at ~ 1.25 V in CV curves compared to the bare SiO_x anode (Fig. 1g), which was consistent with the result of the initial charge/discharge profiles (Fig. S4). For the SiO_x@P anode, the extensively preferential reduction of FEC facilitated the construction of a robust and durable SEI for effective anode protection. Besides, the distinct oxidation peak at ~ 1.25 V was observed (Fig. S4), originating from the delithiation process of Li_3P, which indicated that the Li_3P layer could remain stable on the surface of SiO_x particles during cycling in the cutoff potential range of Si-based anode (below 1.0 V).[35] In contrast, the cathodic peak for SEI formation mainly occurred at 0.55 V for the bare SiO_x since the low FEC adsorption density in IHP could impede the preferred reduction of FEC. During the first discharge process, *ex*-situ FTIR was employed to discern the distinct growth characteristics of the SEI on the SiO_x@P and bare SiO_x (Fig. 1h). Electrolyte had been completely removed before the measurement to exclude its effect on SEI analyses. When discharged to 1.4 V, peaks for poly- or oligomeric (vinylene carbonate) and ($ROCO_2R$) in the 1750–1810 cm^{-1} regions and organophosphorus fluoride ($OPF_{3-y}(OR)_y$) at 903/836 cm^{-1} appeared in the SiO_x@P. However, those peaks were not observed in the FTIR spectrum of the bare SiO_x, indicating that the P surface facilitated the formation of SEI at the higher voltages. Several new adsorption peaks at 1805/1050, 1580/1410/1115, and 1485/710 cm^{-1} were observed in the FTIR spectrum of the SiO_x@P after discharged to 1.0 V, which corresponded to poly(VC), lithium ethylene dicarbonate (LEDC), and Li_2CO_3, respectively.[35-37] These peaks remained constant even at a low discharge voltage of 0.01 V, suggesting that SEI formation primarily occurred in the potential range of 1.4–1.0 V for the SiO_x@P. As a comparison, adsorption peaks for $OPF_{3-y}(OR)_y$ and Li_2CO_3 in the bare SiO_x continued to evolve throughout the discharge process and mainly appeared at 0.01 V instead of 1.4 V. This result supports that SEI formation primarily occurred at a lower potential range of 1.0–0.01 V for the bare SiO_x. All the above results verified the preferential adsorption and reduction of FEC on the SiO_x with P coating, as illustrated in Fig. S5.

2.2 Characterizations of Interface Evolution

To better understand the correlation between SEI chemistry and substrate surface structure, we conducted X-ray photoelectron spectroscopy (XPS) with Ar^+ sputtering depth profiling to reveal the surficial components and their chemical states on the SiO_x@P and bare SiO_x samples after the formation cycle. The high-resolution C *1s* XPS spectra (Fig. 2a) demonstrated four distinct groups of C-C, C-O, CO_3^{2-}, and C-F at 284.8, 286.5, 289.4, and 292.7 eV, respectively (Table S2). These peaks corresponded to the organic species of SEI, including lithium ethylene decarbonate (LEDC), lithium ethyl carbonate (LEC), lithium methyl carbonate (LMC), organophosphorus fluoride, and their oligomers.[38] Compared with the high carbon content of ~ 55% observed for the bare SiO_x after 1200 s Ar^+ sputtering, the SiO_x@P showed much lower carbon content of ~ 30%, implying that the SiO_x@P possessed a much thinner organic-rich layer on the top surface of the SEI in comparison to the bare SiO_x (Fig. 2a). The result was reinforced by observing a persistent C-O peak and a subdued CO_3^{2-} peak in the sputtering of the bare SiO_x electrode. Furthermore, the high-resolution P *2p* XPS spectra (Fig. 2b) for the two samples confirmed the presence of specific decomposition products of anions, such as $Li_xP_yFO_z$ and Li_xPF_y, at ~ 685.6 and ~ 687.3 eV, respectively.[28, 34] Notably, the intensity of these two peaks decreased to background noise levels after 1200 s of sputtering in the SiO_x@P, while they remained almost constant with etching in the bare SiO_x. This result suggested that the repetitive reduction reaction of anions was suppressed by the P functional interface, which could be related to their different adsorption features in the IHP.[18]

Meanwhile, the Li_3P peak at ~ 129.5 eV was shown after 300 s of sputtering, which revealed the lithiation of the P interface layer.[39] In addition, the F *1s* XPS spectra of the SiO_x@P (Fig. 2c) showed dominating peaks for LiF, and they remained over the test time, suggesting the formation of symbiotic Li_3P/LiF-rich SEI. The LiF component in the interphase on the SiO_x@P electrode was mainly derived from the decomposition of FEC. In contrast, the LiF signal faded and almost disappeared after etching for 900 s on the bare SiO_x electrode, suggesting its low content in the SEI. As summarized in Fig. S6, the SiO_x@P displayed higher atomic ratios of F element and proportion of LiF in fluorides (including $Li_xP_yFO_z$/Li_xPF_y, C-F bond, and LiF) than that of the bare SiO_x surface (28% *vs.*11% for F atomic ratio). The *ex-situ* FTIR spectra of the bare SiO_x electrode after the formation cycle still demonstrated the distinct peak at ~ 771 and 1060 cm^{-1} corresponding to the C-F bond, suggesting the incomplete decomposition of FEC,[35] while it disappeared in the SiO_x@P electrode (Fig. S7). These results confirmed that the P functional interface significantly boosted the reduction reaction of FEC through the

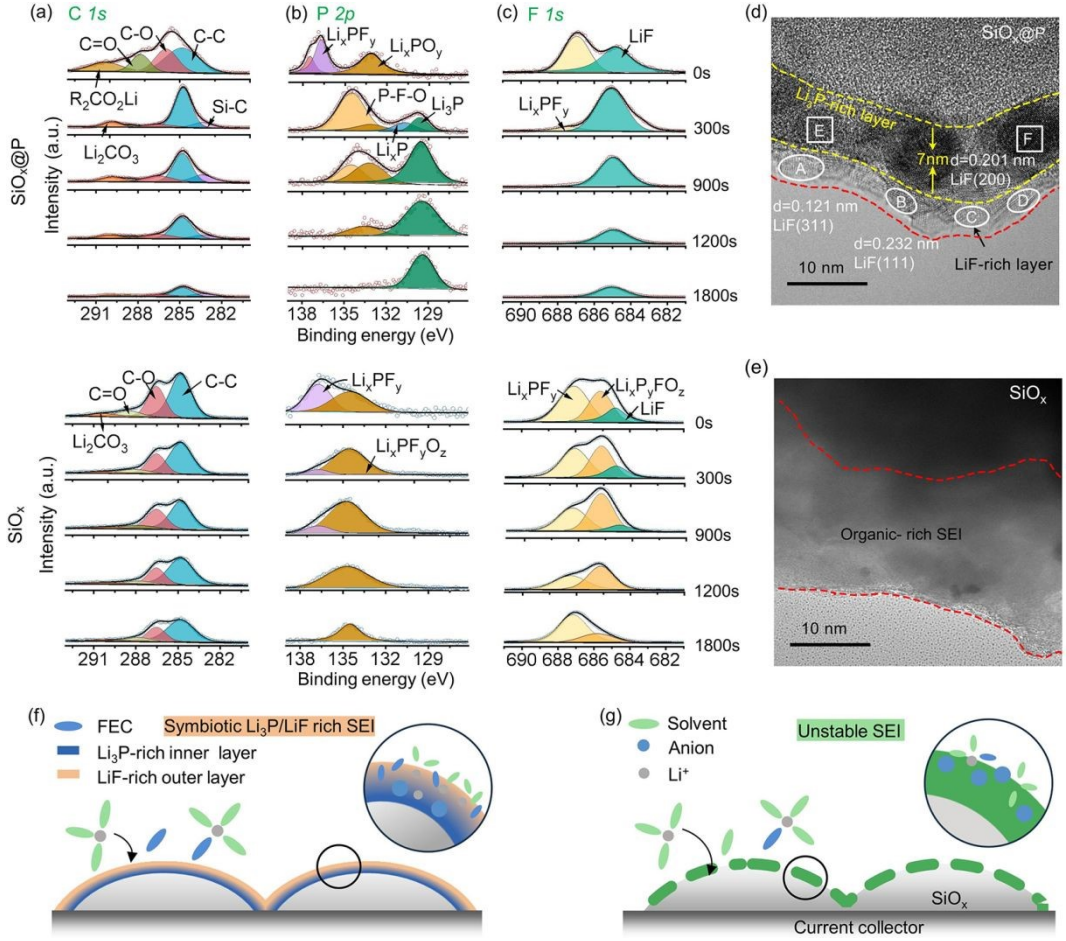

Fig. 2 (a-c) The high-resolution (a) C *1s*, (b) P *2p,* and (c) F *1s*, XPS spectra depth profiles of the SiO_x@P and bare SiO_x after the formation cycle. (d and e) HRTEM images of the SiO_x@P (d) and bare SiO_x (e) after the formation cycle. (f and g) Schematic of the SEI formation on the SiO_x@P (f) and bare SiO_x (g). Selective adsorption and catalytic electrolyte decomposition on the P surface could enable the formation of symbiotic Li_3P/LiF-rich SEI.

enhanced specific adsorption behavior, completely catalytically decomposing the C-F to a high proportion of LiF and promoting the formation of a symbiotic Li_3P/LiF-rich SEI. The high-resolution transmission electron microscopy (HRTEM) image demonstrated that a inorganic-rich SEI with a thickness of ~11 nm was formed on the SiO_x@P. Such a SEI mainly consisted of crystalline inorganic nanoparticles (Fig. 2d), in sharp contrast to the thicker SEI (~16 nm) with amorphous structure on the bare SiO_x (Fig. 2e). The lattice fringes for the crystalline species marked in the outer SEI layer of the SiO_x@P were indexed to (3 1 1), (1 1 1), (2 0 0), (200) crystal planes of LiF, which were evidenced by their *d*-spacing values (0.121, 0.232, 0.201, and 0.201 nm, Fig. S8).[40] The *d*-spacing values of 0.214 and 0.202 nm in the inner SEI layer could be indexed to the (1 1 0) and (1 0 3) crystal planes of the Li_3P nano-domains. [41, 42] A ~7 nm-thick Li_3P-rich sublayer was observed underneath the LiF-rich layer. Besides, the uniform P and F elemental distribution for the as-formed SEI was evidenced by energy-dispersive X-ray spectroscopy (TEM-EDS, Fig. S9). The clear and continuous F and the inside P signals again supported the formation of the symbiotic Li_3P/LiF-based SEI (Fig S9a), as illustrated in Fig. 2f. In contrast, the SEI on bare SiO_x was comprised of scattered inorganics species in the organic substances,

View Article Online
DOI: 10.1039/D4EE00407H

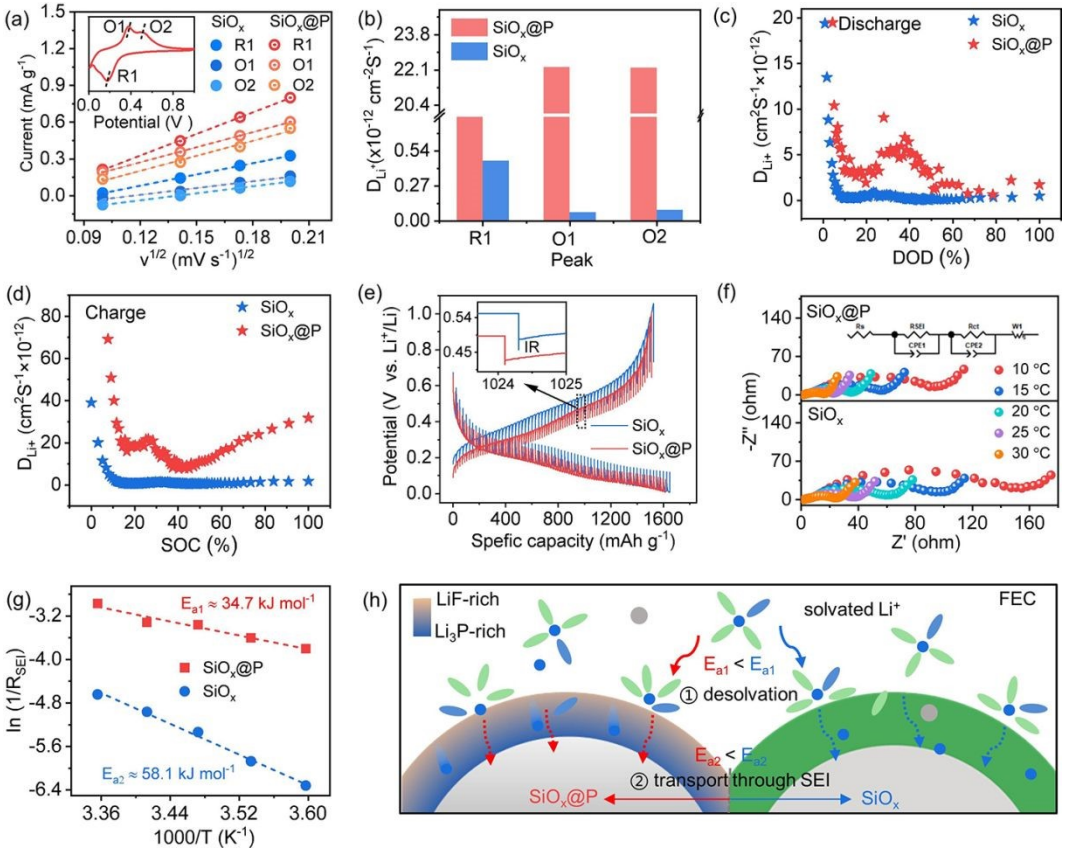

Fig. 3 Electrochemical performance of the SiO_x@P and bare SiO_x electrode in coin cells. (a) The relationship between the square root of the scan rate ($v^{0.5}$) and the peak current density for CV curves of the SiO_x@P and bare SiO_x at different scan rates. The insert is the corresponding cathodic peaks and anodic peaks in SiO_x@P curves. (b) Comparison of the apparent Li^+ diffusion coefficients of R1, O1 and O2 peaks. (c, d) GITT tests for the cells after 5 charge/discharge cycles: Li^+ diffusion coefficients calculated from the 6th (c) discharge and (d) charge profiles, and (e) capacity-potential curves. (f) EIS profiles at different temperatures and the applied equivalent circuit model. (g) Arrhenius behavior and activation energies (E_{a2}) of Li^+ transport through the SEI. (h) Schematic of the enhanced Li^+ transport capability through symbiotic Li_3P/LiF-rich SEI.

as demonstrated in Fig. 2g. In addition, more prominent, distinguished, but intermittent F signals were collected in the SEI formed in the SiO_x electrode (Fig. S9b), corroborating the uneven electrodeposition of electrolyte component-derived fluoride species. The atomic ratio analysis was conducted on the regions marked with the yellow dot line rectangle in the STEM-HADDF (Fig. S10 and Table S3), demonstrating the higher F and P content of the interphase on the SiO_x@P surface compared to the bare SiO_x. To affirm the potency of our proposed mechanism/model in electrolytes encompassing varied FEC concentrations, we pursued a comprehensive exploration of the situation with 5% FEC. The SiO_x@P exhibited an augmented interaction with FEC relative to the uncoated SiO_x, culminating in a superior proportion of LiF within the SEI (Fig. S11). Thus, a high content of FEC is not necessary for the proposed mechanism/model. In brief, the P functional layer in the SiO_x@P can effectively regulate the SEI formation regarding the inorganic species and spatial structure, which could facilitate the electrochemical lithium storage performance under fast charging conditions (Fig. S12).

2.3 Li^+ transport kinetics for SiO_x@P with symbiotic Li_3P/LiF-rich SEI

The Li^+ diffusion behaviors and interfacial kinetics properties of SiO_x@P with symbiotic Li_3P/LiF-rich SEI were studied by CV, galvanostatic electrochemical impedance spectroscopy (EIS), and intermittent titration technique (GITT) methods. The CV curves were recorded at different scan rates ranging from 0.01 to 0.04 mV s^{-1} (Fig. S13). The cathodic peaks (R1) at ~ 0.12 V originated from the lithiation of Si to produce lithium silicide (Li_xSi), while the two anodic peaks (O1 and O2) at ~ 0.34 and 0.50 V corresponding to the reversible transformation from Li_xSi to amorphous Si.[43] The corresponding peak currents showed a linear relationship with the square root of scanning rates (Fig. 3a), suggesting the diffusion-limited alloying reaction. Therefore, the Li^+ diffusion coefficients could be calculated by the Randles-Sevcik equation:[44]

$$Ip = 2.69 \times 10^5 n^{1.5} A D_{Li}^{0.5} C_{Li} v^{0.5} \quad (a)$$

Where I_p, n, A, D_{Li} (including D_{Li}^{IpR1}, D_{Li}^{IpO1}, and D_{Li}^{IpO1}), v and C_{Li} is the peak current, the number of transfer electrons, the active electrode area, the Li^+ diffusion coefficient, the concentration of Li^+ in the electrolyte, and the scan rate, respectively. The calculated apparent Li^+ diffusion coefficients of R1, O1, and O2 peaks were recorded in

View Article Online
DOI: 10.1039/D4EE00407H

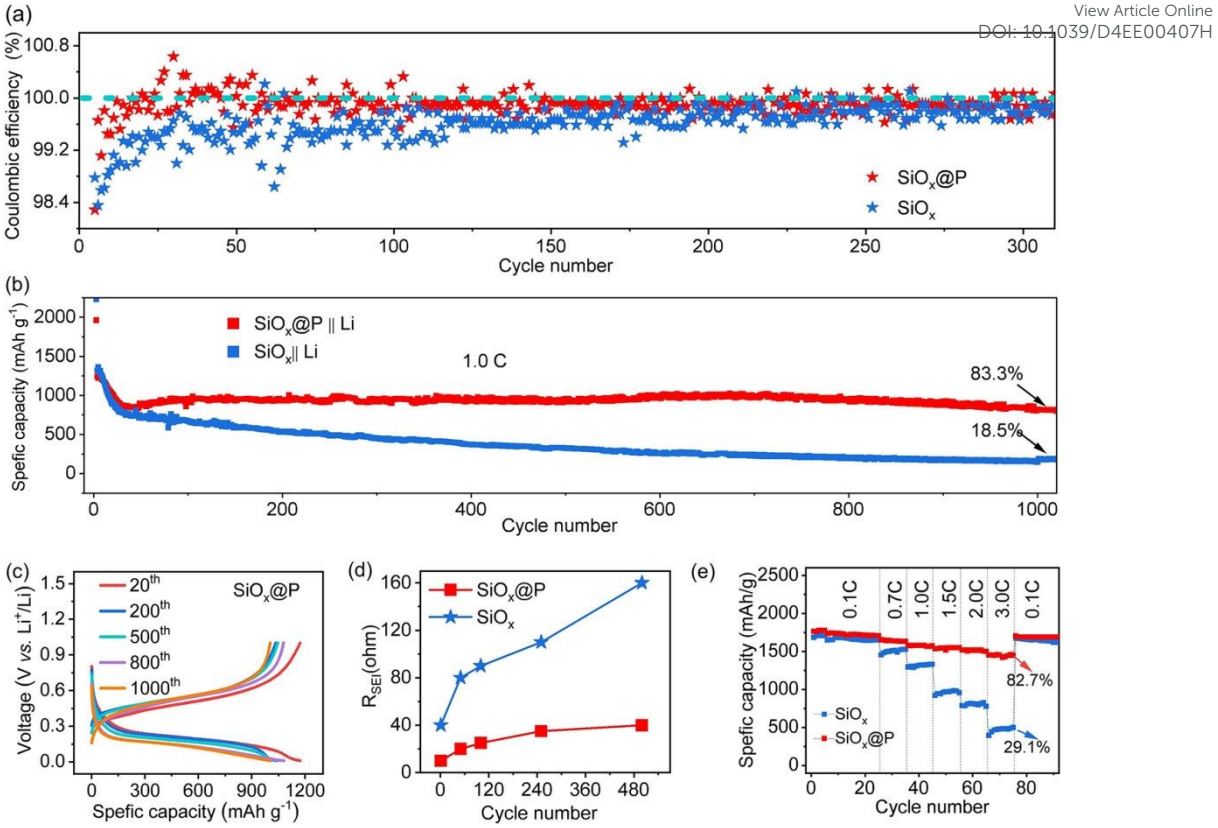

Fig. 4 (a) CE-cycle number plots, (b) capacity-cycle number plots, and (c) the corresponding galvanostatic charging/discharging profiles of the SiO_x@P Li and SiO_x Li cells. (d) Comparison of R_{SEI} against cycle numbers for the cycled SiO_x and SiO_x@P electrodes. (e) Rate performance of the SiO_x@P Li and SiO_x Li cells.

Fig. 3b. The corresponding values of the SiO_x@P were higher than that of the bare SiO_x in both the oxidation and reduction processes, which could be ascribed to the high ionically conductive SEI of Li_3P crystallites and crystal boundaries' synergetic effects of symbiotic Li_3P/LiF.[45] Moreover, the D_{Li^+} value based on GITT (Fig. 3c, d) for the SiO_x@P was much higher than the bare SiO_x, again supporting its fast Li^+ transport capability. The significantly increased IR drop under excitation-relaxation cycles reflected the increased cell polarization of the bare SiO_x, in contrast to the low value of the SiO_x@P (Fig. 3e). The Li^+ transport capability through SEI (R_{SEI}) and the charge transfer resistance (R_{ct}) were investigated by temperature-dependent EIS (Fig. 3f), and the corresponding activation energy was calculated based on the Arrhenius law according to the EIS results.[46] As shown in Fig. 3g, h and S13c, the activation energy of the desolvation process (E_{a1}) and Li^+ transport through symbiotic Li_3P/LiF-rich SEI (E_{a2}) were much lower than that for the bare SiO_x, further indicating that the symbiotic Li_3P/LiF-based SEI significantly improved the Li^+ migration kinetics, which is highly dependent on the SEI properties (41.7 vs. 65.1 kJ mol^{-1} for E_{a1}, 34.7 *vs*. 58.1 kJ mol^{-1} for E_{a2}). [10, 47, 48] The above advantages primarily resulted from the existence of Li_3P, which exhibited strong affinity energy and higher ionic conductivity for Li^+ ions than the conventional SEI components, including LMC, LEMC, Li_2CO_3, Li_2O, and LiF, as summarized in Table S5.[49] The former characteristic can be advantageous for Li^+ ion desolvation at the electrode surface, while the latter facilitates rapid Li^+ ion transport within the SEI. These properties collectively enable fast electrochemical reaction kinetics of the symbiotic Li_3P/LiF-rich SEI.

2.4 Electrochemical Performance

The electrochemical performance of the SiO_x@P electrode with symbiotic Li_3P/LiF-rich SEI was first measured with a Li metal half-cell configuration. The CE of the SiO_x@P quickly reached 99.95% after only 20 cycles (Fig. 4a), indicating that the parasitic reaction between the electrolyte and active material on cycling was significantly suppressed due to the formation of robust symbiotic Li_3P/LiF-dominated SEI. By contrast, the CE of the bare SiO_x slightly increased from 90.2% to 99.3% after 20 cycles and remained constant during the following cycles. The inferior CE of the bare SiO_x over cycling exhibited the continuous parasitic reaction between active material and electrolyte, leading to fast electrochemical performance decay. The SiO_x@P showed impressive long-term cycling stability and a meager capacity decay rate of 16.7% from 30 to 1000 cycles after its stabilization (Fig. 4b, c, and Fig. S14). In contrast, the bare SiO_x displayed continuous capacity decay on cycling, and the capacity retention was only 18.5% after 1000 cycles at the same test condition (Fig. S15). Besides, even under high mass loading (~ 3.5 mg cm^{-2}) of the active materials, the SiO_x@P still showed a negligible capacity decay on cycling and delivered a high reversible areal capacity of 3.5 mAh cm^{-2} for 500 cycles (Fig. S16c). Note that the results were achieved in the electrolyte with optimized FEC content (Fig. S17). The R_{SEI} and R_{ct} of the SiO_x@P electrodes were smaller than the bare SiO_x electrodes (larger than 60 Ω) after long-term cycling (Fig. 4d and Fig. S19). They remained almost unchanged while the R_{ct} of the bare SiO_x electrode increased with the cycling numbers (ranging from 80 Ω at

the 50th cycle to 250 Ω at the 500th cycle). These results demonstrated the success of the symbiotic Li_3P/LiF-rich SEI construction in enabling long-cycle stable Si-based electrodes. In addition to the stable cycle performance, the SiO_x@P demonstrated a reversible capacity of 1450 mAh g^{-1} at 3.0 *C* (4.5 A g^{-1}, active materials loading ~ 0.21 mg cm^{-2}) and exhibited excellent rate capability (Fig. 4e and Figs. S20,21). By contrast, the bare SiO_x lost almost all its capacity and showed less than 400 mAh g^{-1} under the same testing condition. After cycling at high rates, the capacity of the SiO_x@P was recovered to 1689.6 mAh g^{-1} when the current density switched back to 0.2 *C*. However, the bare SiO_x exhibited remarkably reduced lithium storage capacity at the same test condition, which should be ascribed to the ever-accumulated SEI and slow Li^+ transport kinetics.

To explain the excellent electrochemical stability of the SiOx@P, the cross-section SEM images for both electrodes before and after 100 charge/discharge cycles were investigated (Fig. 5a, b). The SiO_x@P electrode showed a low swelling rate of ~ 29.1% in thickness in sharp contrast of ~ 61.3% for the bare SiO_x electrode (40 µm vs. 50 µm after cycling, Fig. 5c). Such a result could be attributed to the suppressed parasitic reaction between the active material and electrolyte for the SiO_x@P, where the undesirable continuous accumulation of by-products would not occur during long-term cycling.[50] The high inorganic contents of LiF and Li_3P enhanced the mechanical stability of the SEI, which was probed by atomic force microscopy (AFM). The cycled SiO_x@P electrodes exhibited a smooth surface with low roughness, while the bare SiO_x electrode surface was relatively coarse (Fig. 5d, e). The Young's modulus of the SiO_x@P was found to be higher than that of the bare SiO_x (3.2 GPa *vs*. 0.9 GPa, Fig. 5f, g and S22), demonstrating the outstanding mechanical properties of the symbiotic Li_3P/LiF-rich SEI. Based on the investigation by Guo *et al.*, the resultant force-displacement curve can be divided into several segments, and the elastic strain limit is an appropriate indicator to evaluate the tolerance of SEI towards volume expansion.[49] As shown in Fig. 5h, i, the SEI derived from the SiO_x@P surface was thinner and had a higher maximum elastic deformation limit compared to that on the bare SiO_x surface (22 *vs.* 31 nm for the SEI thickness and 5 *vs.* 4 nm for the maximum elastic deformation limit) after 100 charge/discharge cycles. Based on the above results, it is concluded that the formation of symbiotic Li_3P/LiF-rich SEI on the SiO_x@P enabled stable materials structure and suppressed parasitic reactions between active materials and electrolyte on cycling, in contrast to the rapid decay in electrochemical performance and materials structure for bare SiO_x with a thick and organic-rich SEI.

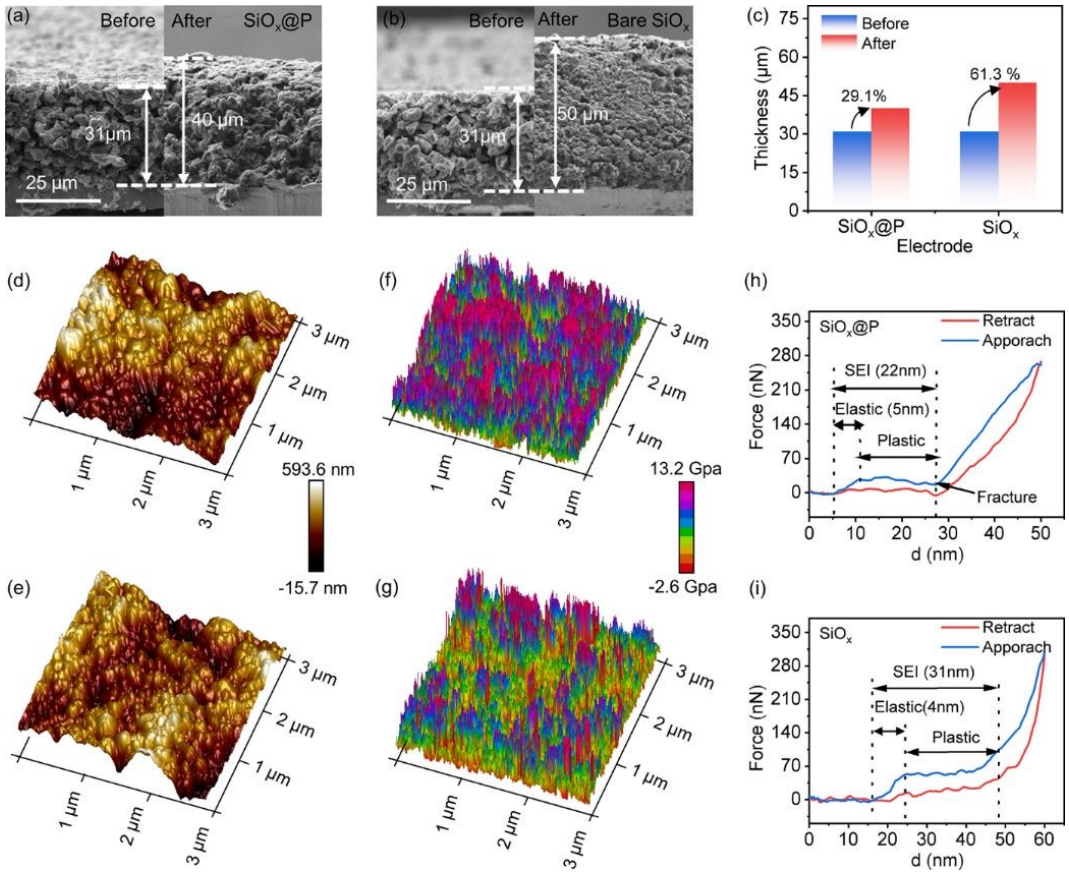

Fig. 5 (a-c) SEM images of the cross-section of the SiO_x@P (a) and the bare SiO_x electrodes (b) before and after 100 charge/discharge cycles at 1.0 *C*, and (c) comparison of the thickness variation and swelling rate of both electrodes. (d, e) Typical AFM morphology and (f, g) Young's modulus comparison of the SEI in the SiO_x@P and bare SiO_x anodes after 100 charge/discharge cycles at 1.0 *C*. (h, i) Force-displacement curves.

View Article Online
DOI: 10.1039/D4EE00407H

To show the fast-charging capability of SiO_x@P anode, a single-layer pouch cell paired with NCM622 cathode was fabricated. Notably, the NCM622||SiO_x@P pouch cell demonstrated outstanding performance, achieving 86.5 % and 81.2% of the capacity at 4 *C* and 6 *C* charging rates (corresponding to charging time of 15 minutes and 10 minutes), respectively, compared to the capacity at 0.2 *C* (~ 91.6 mAh, ~178 mAh g^{-1} based on NCM622). By contrast, only 41.4% of the capacity was achieved at the charging rate of 6 *C* for the NCM622||SiO_x pouch cell at 0.2 *C* (~ 88.2 mAh, 175 mAh g^{-1}, Fig. 6a). To show the enhanced fast-charging capability of the SiO_x@P anode, we compared the voltage polarization of both cells under 4 *C* charging conditions. In contrast to the SiO_x@P -based pouch cells, the bare SiO_x-based cells quickly reached the cutoff voltage (6 minutes increased up to 4.2V), accompanied by significant polarization. The indicative median voltage difference values for the cells were ~0.39 V for SiO_x@P and 0.69 V for SiO_x, identified as the primary cause of rate capability decay (Figs. 6b and S23, S24). Achieving cycling stability during fast-charging conditions is a crucial parameter for the practical integration of fast-charging batteries. As shown in Fig. 6c and d, an incomparable cycle lifespan of 300 cycles with 83.2% capacity retention was achieved at 4 *C* for the SiO_x@P-based pouch cell. In contrast, the cells with the bare SiO_x exhibited a much lower capacity retention of 65.4% after 100 cycles at 4 *C*. Moreover, compared to the bare SiO_x, SiO_x@P showcased lower overpotential and polarization during cycling. At the 200th cycle, the median voltage difference was approximately 0.42 V for the NCM622|| SiO_x@P cell, while it amounted to 0.71 V for the NCM622||SiO_x pouch cell (Fig. S25-27). This accounted for the enhanced Coulombic efficiency and excellent electrochemical performance throughout the cycling process for SiO_x@P.

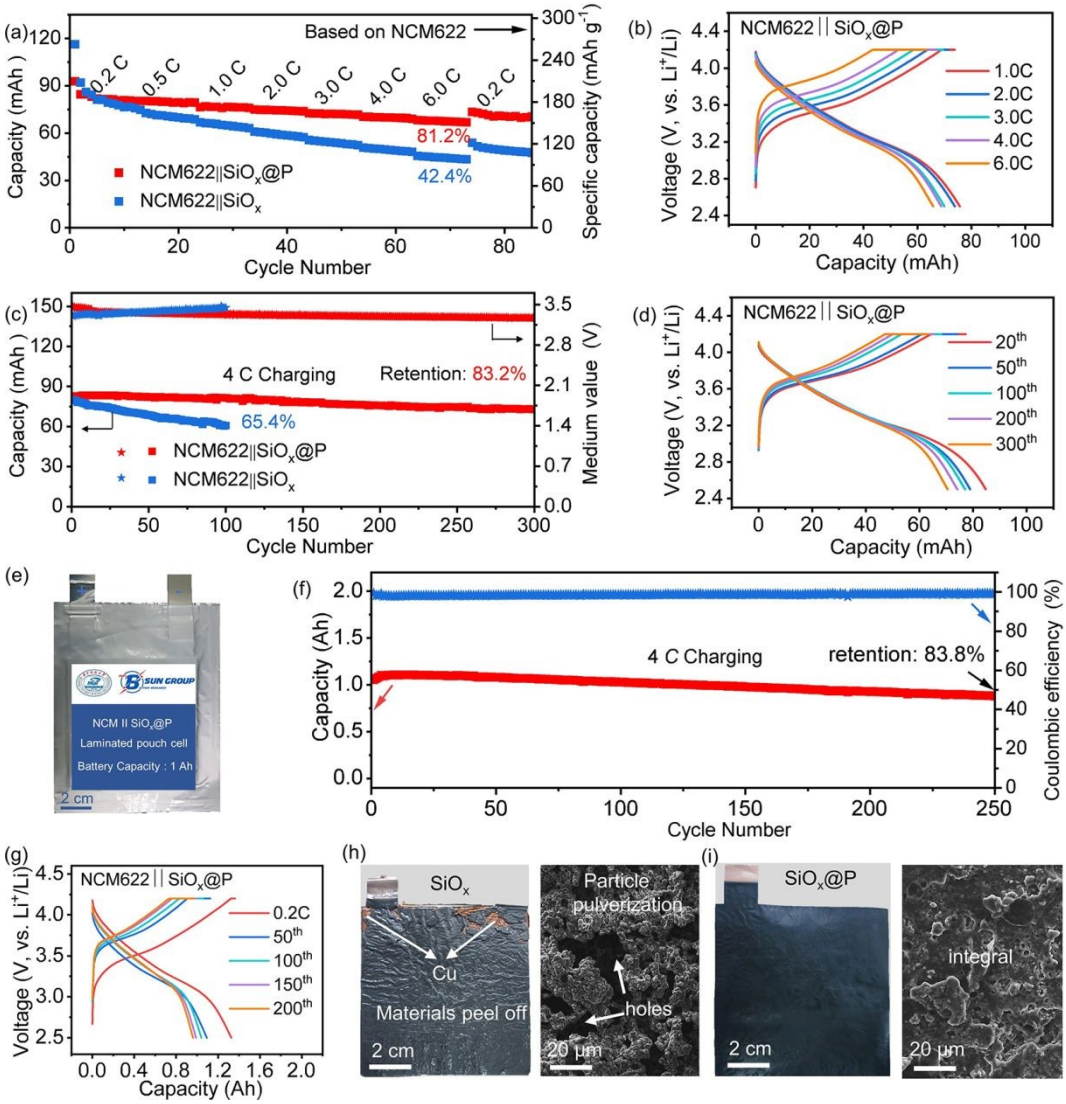

Fig. 6 (a and b) Cycling performance of the pouch cells with different SiO_x anodes (a), and the charging/discharging profiles of the pouch cell with SiO_x@P anode under different charging rates (0.2 to 6 *C*) (b). (c and d) Cycling performance of the pouch cells with different SiO_x anodes (c), and the charging/discharging profiles of the pouch cell with SiO_x@P anode at a charging rate of 4 *C* (d). (e) Photograph of the NCM622||SiO_x@P laminated pouch cell. (f and g) Cycling performance (f) and the corresponding charging/discharging voltage profiles of the NCM622||SiO_x@P laminated pouch cell at a charging rate of 4 *C* for different cycles (g). (h and i) The optical and top-view SEM images of bare SiO_x (h) and SiO_x@P anodes (i). The discharging rate for all the cells was fixed at 0.2 *C*.

To further elucidate the practical application of the SiO_x@P anode for fast-charging lithium-ion batteries with high energy density, an Ah-level NCM622||SiO_x@P pouch cell was meticulously assembled (Fig. 6e, Table S4). As anticipated, the cell demonstrated exceptional electrochemical performance, delivering a reversible capacity of 1.3 Ah at 0.2 *C* (an impressive high energy density of 410 Wh kg^{-1} and 780 Wh L^{-1}). Notably, 86.5 % of the capacities were maintained at the charging rate of 4 *C* (a high power density of 1404 W kg^{-1} and 2720 W L^{-1}). Moreover, it achieved remarkable capacity retention of ~83.8% after 250 cycles under a 4 *C* charging rate, underscoring its superior electrochemical cycling stability under fast-charging conditions (Fig. 6 e-g). In addition, we investigated the morphology and microstructure evolution of the SiO_x@P electrode upon cycling, gaining insights into the stability of the as-converted inorganic component on the SiO_x surface in a pouch full cell after long-term cycling under fast charging. The TEM images revealed a stable, crystalline symbiotic Li_3P/LiF-rich SEI with a thickness of ~25 nm after prolonged cycles of fast charging, which was similar to the initial SiO_x@P anode. Importantly, the particles remained intact without breakage (Figs. S28 and S29). Further analysis through TEM-EDS showed a fluorine (F) layer covering P signals on the SiO_x@P particles, affirming the existence of a symbiotic Li_3P/LiF-rich SEI on the SiO_x@P surface (Fig. S30). These findings validate the excellent chemical and electrochemical stability of the Li_3P/LiF symbiotic SEI, effectively suppressing continuous electrolyte decomposition and byproduct accumulation on the electrode surface during long-term cycling under fast charging conditions.

Moreover, the cycled bare SiO_x anode exhibited obvious particle pulverization and material peeling off from the current collector, accompanied by buckling, puckering, and tearing of the current collector (Fig. S31). These observations suggested an electrochemical-mechanical mismatch/instability under fast-charging conditions, potentially contributing to the degradation of electrochemical performance. In contrast, the surface of the cycled SiO_x@P anode, along with the underlying copper foil, exhibited a compact and integral morphology, indicating the robust electrochemical-mechanical property of the materials' particles and the SEI. This observation underscores the realization of superior electrochemical-mechanical stability during cycling, even under harsh, fast-charging conditions with enormous structural stress. Therefore, the SiO_x@P anode enabled the formation of dense Li_3P/LiF symbiotic SEI featuring high stability and ionic conductivity, prolonged the cycling lifespan, and promoted the realization of superior fast charging capability of LIBs with high energy density.

Conclusions

In general, we revealed that interphase structure could play a significant role in the formation of SEI and regulate the electrochemical performance of a high-capacity Si-based anode. By introducing a functional P interphase layer, a robust Li_3P/LiF-rich SEI was successfully constructed on the SiO_x surface through its specific adsorption with the FEC additive in IHP, and it improved the mechanical and electrochemical stability during the repeated charge/discharge processes. As a result, the SiO_x@P showed remarkable improvement in terms of CE, rate capability, and cycle stability compared to the bare SiO_x. This work has shed light on utilizing surface engineering to tailor the composition and mechanical properties of the SEI and may boost advanced SEI design for high-energy-density LIBs with fast charging capability.

Author Contributions

Kai Cheng: Conceptualization, Investigation, Data curation, Methodology, and Writing - original draft. Shuibin Tu: Investigation, Methodology, and Editing. Bao Zhang: Investigation and Methodology. Wenyu Wang: Data curation. Xiaohong Wang: Data curation. Yucheng Tan: Data curation. Xiaoxue Chen: Data curation. Chunhao Li: Data curation. Chenhui Li: Data curation, Methodology. Li Wang: Editing, and Yongming Sun: Supervision, Conceptualization, Methodology, Writing - review and editing. All authors discussed and contributed to the results.

Conflicts of interest

The authors declare no competing financial interest.

Acknowledgments

Y.S. acknowledges the support from the Natural Science Foundation of China (grant no. 52072137). The Analytical and Testing Center of Huazhong University of Science and Technology (HUST) was acknowledged for providing the facilities for the characterization of materials.

Experimental Section

Detailed experimental procedures can be found in the Supporting Information.

References

1. Y. F. Tian, G. Li, D. X. Xu, Z. Y. Lu, M. Y. Yan, J. Wan, J. Y. Li, Q. Xu, S. Xin, R. Wen and Y. G. Guo, *Adv Mater*, 2022, **34**, e2200672.
2. L. Zhang, Q. Huang, X. Liao, Y. Dou, P. Liu, M. Al-Mamun, Y. Wang, S. Zhang, S. Zhao, D. Wang, G. Meng and H. Zhao, *Energy & Environmental Science*, 2021, **14**, 3502-3509.
3. S. Wu, K. Zhu, J. Tang, K. Liao, S. Bai, J. Yi, Y. Yamauchi, M. Ishida and H. Zhou, *Energy & Environmental Science*, 2016, **9**, 3262-3271.
4. L. Zhou, Z. Zhuang, H. Zhao, M. Lin, D. Zhao and L. Mai, *Advanced Materials*, 2017, **29**.
5. D. Zhuang, Y. Zhang, R. He, J. Ren, Q. Li, L. Mai and L. Zhou, *Materials Chemistry Frontiers*, 2023, **7**, 3650-3656.
6. Q. Y. Zhenhui Liu, Yunlong Zhao, Ruhan He, Ming Xu, Shihao Feng, Shidong Li, Liang Zhou and Liqiang Mai, *Chem. Soc. Rev.*, 2019, **48**, 285.
7. J.-I. Lee, Y. Ko, M. Shin, H.-K. Song, N.-S. Choi, M. G. Kim

and S. Park, *Energy & Environmental Science*, 2015, **8**, 2075-2084.
8. H. Du, R. Yu, X. Tan, J. Wu, D. Zhao, L. Mai and L. Zhou, *Science China Materials*, 2023, **66**, 2199-2206.
9. S. Pan, J. Han, Y. Wang, Z. Li, F. Chen, Y. Guo, Z. Han, K. Xiao, Z. Yu, M. Yu, S. Wu, D. W. Wang and Q. H. Yang, *Adv Mater*, 2022, **34**, e2203617.
10. X. Zheng, Z. Gu, J. Fu, H. Wang, X. Ye, L. Huang, X. Liu, X. Wu, W. Luo and Y. Huang, *Energy & Environmental Science*, 2021, **14**, 4936-4947.
11. W. Deng, X. Yin, W. Bao, X. Zhou, Z. Hu, B. He, B. Qiu, Y. S. Meng and Z. Liu, *Nature Energy*, 2022, **7**, 1031-1041.
12. P. Shi, F. Liu, Y. Feng, J. Zhou, X. Rui and Y. Yu, *Small*, 2020, **16**, e2001989.
13. N. Qin, L. Jin, Y. Lu, Q. Wu, J. Zheng, C. Zhang, Z. Chen and J. P. Zheng, *Advanced Energy Materials*, 2022, **12**.
14. S. Chae, W.-J. Kwak, K. S. Han, S. Li, M. H. Engelhard, J. Hu, C. Wang, X. Li and J.-G. Zhang, *ACS Energy Letters*, 2021, **6**, 387-394.
15. Z. Cao, X. Zheng, M. Zhou, T. Zhao, L. Lv, Y. Li, Z. Wang, W. Luo and H. Zheng, *ACS Energy Letters*, 2022, **7**, 3581-3592.
16. C. Qian, J. Zhao, Y. Sun, H. R. Lee, L. Luo, M. Makaremi, S. Mukherjee, J. Wang, C. Zu, M. Xia, C. Wang, C. V. Singh, Y. Cui and G. A. Ozin, *Nano Letters*, 2020, **20**, 7455-7462.
17. Y.-S. Hu and Y. Lu, *ACS Energy Letters*, 2020, **5**, 3633-3636.
18. C. Yan, H. R. Li, X. Chen, X. Q. Zhang, X. B. Cheng, R. Xu, J. Q. Huang and Q. Zhang, *J Am Chem Soc*, 2019, **141**, 9422-9429.
19. B. Q. Xiong, X. Zhou, G. L. Xu, Y. Liu, L. Zhu, Y. Hu, S. Y. Shen, Y. H. Hong, S. C. Wan, X. C. Liu, X. Liu, S. Chen, L. Huang, S. G. Sun, K. Amine and F. S. Ke, *Advanced Energy Materials*, 2019, **10**.
20. W. Song, E. S. Scholtis, P. C. Sherrell, D. K. H. Tsang, J. Ngiam, J. Lischner, S. Fearn, V. Bemmer, C. Mattevi, N. Klein, F. Xie and D. J. Riley, *Energy & Environmental Science*, 2020, **13**, 4977-4989.
21. L. Huang, H. Fu, J. Duan, T. Wang, X. Zheng, Y. Huang, T. Zhao, Q. Yu, J. Wen, Y. Chen, D. Sun, W. Luo and Y. Huang, *Chem*, 2022, **8**, 1928-1943.
22. S. Tu, Z. Lu, M. Zheng, Z. Chen, X. Wang, Z. Cai, C. Chen, L. Wang, C. Li, Z. W. Seh, S. Zhang, J. Lu and Y. Sun, *Adv Mater*, 2022, **34**, e2202892.
23. C. Liu, M. Han, Y. Cao, L. Chen, W. Ren, G. Zhou, A. Chen and J. Sun, *Energy Storage Materials*, 2021, **37**, 417-423.
24. H. Wang, C. Liu, H. Wang, X. Han, S. Zhang, J. Sun, Y. Zhang, Y. Cao, Y. Yao and J. Sun, *Chem Commun (Camb)*, 2021, **57**, 3975-3978.
25. M. Li, W. Li, Y. Hu, A. A. Yakovenko, Y. Ren, J. Luo, W. M. Holden, M. Shakouri, Q. Xiao, X. Gao, F. Zhao, J. Liang, R. Feng, R. Li, G. T. Seidler, F. Brandys, R. Divigalpitiya, T. K. Sham and X. Sun, *Adv Mater*, 2021, **33**, e2101259.
26. J. Xu, J. Zhang, T. P. Pollard, Q. Li, S. Tan, S. Hou, H. Wan, F. Chen, H. He, E. Hu, K. Xu, X. Q. Yang, O. Borodin and C. Wang, *Nature*, 2023, **614**, 694-700.
27. S. Y. Sun, N. Yao, C. B. Jin, J. Xie, X. Y. Li, M. Y. Zhou, X. Chen, B. Q. Li, X. Q. Zhang, and Q. Zhang, *Angew Chem Int Ed Engl*, 2022, **61**, e202208743.
28. J. Hao, F. Yang, S. Zhang, H. He, G. Xia, Y. Liu, C. Didier, T. Liu, W. K. Pang, V. K. Peterson, J. Lu, and Z. Guo, *Proceedings of the National Academy of Sciences*, 2020, **117**, 2815-2823.
29. T. Liu, L. Lin, X. Bi, L. Tian, K. Yang, J. Liu, M. Li, Z. Chen, J. Lu, K. Amine, K. Xu and F. Pan, *Nature Nanotechnology*, 2018, **14**, 50-56.
30. Y. Horowitz, H. L. Han, F. A. Soto, W. T. Ralston, P. B. Balbuena and G. A. Somorjai, *Nano Lett*, 2018, **18**, 1145-1151.
31. L. H. Shao, J. Biener, D. Kramer, R. N. Viswanath, T. F. Baumann, A. V. Hamza and J. Weissmuller, *Phys Chem Chem Phys*, 2010, **12**, 7580-7587.
32. G. V. Bossa, D. L. Z. Caetano, S. J. de Carvalho and S. May, *Electrochimica Acta*, 2019, **321**.
33. B. N. Olana, L. H. Adem, S. D. Lin, B.-J. Hwang, Y.-C. Hsieh, G. Brunklaus and M. Winter, *ACS Applied Energy Materials*, 2023, **6**, 4800-4809.
34. M. Nie, D. Chalasani, D. P. Abraham, Y. Chen, A. Bose and B. L. Lucht, *The Journal of Physical Chemistry C*, 2013, **117**, 1257-1267.
35. V. Etacheri, O. Haik, Y. Goffer, G. A. Roberts, I. C. Stefan, R. Fasching and D. Aurbach, *Langmuir*, 2012, **28**, 965-976.
36. R. Jorn, R. Kumar, D. P. Abraham and G. A. Voth, *The Journal of Physical Chemistry C*, 2013, **117**, 3747-3761.
37. N. N. Intan and J. Pfaendtner, *ACS Appl Mater Interfaces*, 2021, **13**, 8169-8180.
38. C. Marino, M. El Kazzi, E. J. Berg, M. He and C. Villevieille, *Chemistry of Materials*, 2017, **29**, 7151-7158.
39. R. Reinhold, U. Stoeck, H. J. Grafe, D. Mikhailova, T. Jaumann, S. Oswald, S. Kaskel and L. Giebeler, *ACS Appl Mater Interfaces*, 2018, **10**, 7096-7106.
40. W. Huang, J. Wang, M. R. Braun, Z. Zhang, Y. Li, D. T. Boyle, P. C. McIntyre, and Y. Cui, *Matter*, 2019, **1**, 1232-1245.
41. J. Li, D. Liu, H. Sun, D. Qu, Z. Xie, H. Tang and J. Liu, *SmartMat*, 2023, DOI: 10.1002/smm2.1200.
42. S. X. Hongchang Jin, Chenghao Chuang, Wangda Li, Haiyun Wang, Jian Zhu, Huanyu Xie, Taiming Zhang, Yangyang Wan, Zhikai Qi, Wensheng Yan, Ying-Rui Lu, Ting-Shan Chan, Xiaojun Wu, John B. Goodenough, Hengxing Ji, Xiangfeng Duan, *Science* 2020, **370**, 192–197
43. Q. Xu, J. K. Sun, Z. L. Yu, Y. X. Yin, S. Xin, S. H. Yu and Y. G. Guo, *Adv Mater*, 2018, **30**, e1707430.
44. Z. Li, W. Tang, Y. Yang, G. Lai, Z. Lin, H. Xiao, J. Qiu, X. Wei, S. Wu and Z. Lin, *Advanced Functional Materials*, 2022, **32**.
45. T. Kang, J. Tan, X. Li, J. Liang, H. Wang, D. Shen, Y. Wu, Z. Huang, Y. Lu, Z. Tong and C.-S. Lee, *Journal of Materials Chemistry A*, 2021, **9**, 7807-7816.
46. SutingWeng, X. Zhang, G. Yang, S. Zhang, B. Ma, Q. Liu, Y. Liu, C. Peng, H. Chen, H. Yu, X. Fan, T. Cheng, L. Chen, Y. Li, Z. Wang and X. Wang, *Nature Communications*, 2023, **14**.
47. X. Zheng, Z. Cao, W. Luo, S. Weng, X. Zhang, D. Wang, Z. Zhu, H. Du, X. Wang, L. Qie, H. Zheng and Y. Huang, *Advanced Materials*, 2023, **35**.
48. X. Zheng, L. Huang, X. Ye, J. Zhang, F. Min, W. Luo and Y. Huang, *Chem*, 2021, **7**, 2312-2346.
49. S. Tu, B. Zhang, Y. Zhang, Z. Chen, X. Wang, R. Zhan, Y. Ou, W. Wang, X. Liu, X. Duan, L. Wang and Y. Sun, *Nature Energy*, 2023, **8**, 1365-1374.
50. Z. Cao, X. Zheng, Y. Wang, W. Huang, Y. Li, Y. Huang and H. Zheng, *Nano Energy*, 2022, **93**.